Tunneling with a hydrodynamic pilot-wave model

André Nachbin,[1,3] Paul A. Milewski,[2] and John W. M. Bush[3]
[1]*IMPA, Estrada Dona Castorina 110, Rio de Janeiro, Rio de Janeiro 22460-320, Brazil*
[2]*Department of Mathematical Sciences, University of Bath, Bath BA2 7AY, United Kingdom*
[3]*Department of Mathematics, MIT, 77 Massachusetts Avenue, Cambridge, Massachusetts 02139, USA*
(Received 28 April 2016; published 30 March 2017)

Eddi *et al.* [Phys. Rev Lett. **102**, 240401 (2009)] presented experimental results demonstrating the unpredictable tunneling of a classical wave-particle association as may arise when a droplet walking across the surface of a vibrating fluid bath approaches a submerged barrier. We here present a theoretical model that captures the influence of bottom topography on this wave-particle association and so enables us to investigate its interaction with barriers. The coupled wave-droplet dynamics results in unpredictable tunneling events. As reported in the experiments by Eddi *et al.* and as is the case in quantum tunneling [Gamow, Nature (London) **122**, 805 (1928)], the predicted tunneling probability decreases exponentially with increasing barrier width. In the parameter regimes examined, tunneling between two cavities suggests an underlying stationary ergodic process for the droplet's position.

DOI: 10.1103/PhysRevFluids.2.034801

I. INTRODUCTION

Eddi *et al.* [1] presented the results of an investigation of the tunneling of a walking droplet (henceforth a "walker") interacting with a submerged barrier. The work [1] demonstrated that "this wave-particle association has a nonlocality sufficient to generate a quantumlike tunneling at a macroscopic scale" (p. 240401-1). The authors show that the reflection and transmission of a walker over a submerged barrier is unpredictable. Moreover, they demonstrate that the crossing probability decreases exponentially with increasing barrier width, as in the case of quantum tunneling [2]. This hydrodynamic tunneling has not previously been examined theoretically owing to the difficulties in treating variable bottom topography. It will be studied here in a one-dimensional (1D) configuration with a reduced theoretical model; specifically, the free surface is one dimensional while the fluid body is two dimensional. This reduced model yields an explicit set of differential equations for the wave-particle association in confined domains.

We here present a system of partial differential equations obtained from a systematic reduction of the Navier-Stokes equations, leading to a hydrodynamic pilot-wave model in a confined domain. This potential theory model includes the feedback between the droplet and its guiding pilot-wave while adequately accounting for general bottom topographies. Recently, Pucci *et al.* [3] examined the nonspecular reflection of walking droplets for a planar barrier. Numerical simulations were performed with a nearly monochromatic model developed by Faria [4], which simplifies potential theory at a given wave number, corresponding to the Faraday mode. The potential theory model, here presented, captures probabilistic features of tunneling as observed in laboratory experiments [1]. The model also yields statistics for the droplet position that indicate an underlying stationary ergodic process, as was reported by Harris *et al.* [5] in their experimental investigation of a walker in a circular corral.

Consider a fluid bath oscillating vertically at frequency ω_0. In the bath's reference frame, the acceleration is $g(t) = g[1 + \Gamma \sin(\omega_0 t)]$, where g is the gravitational acceleration and Γ is the forcing amplitude. The fluid is quiescent for $\Gamma < \Gamma_F$, where Γ_F is the Faraday threshold. When $\Gamma \geqslant \Gamma_F$ a subharmonic instability takes place, leading to standing Faraday waves with the Faraday wavelength λ_F, as is prescribed by the water-wave dispersion relation [6]. Walker [7] demonstrated that a millimetric droplet can bounce indefinitely on the surface of a vertically oscillating bath.

Couder and coauthors [1,8] discovered that when the parameter Γ exceeds the walking threshold Γ_w the bouncing droplet becomes unstable to lateral perturbations and executes horizontal motion [9]. In this walking regime $\Gamma_w < \Gamma < \Gamma_F$, the droplet bounces every two bath cycles, so with frequency $\omega_0/2$, thereby achieving resonance with its Faraday wave field. The droplet is then guided by its underlying pilot-wave, a spatially extended monochromatic wave field with a Faraday period $T_F = \omega_0/2$ [6]. We note that while Γ is always below Γ_F, the bouncing droplet locally triggers the subharmonic, most unstable Faraday wave mode [9,10].

Central to the walker dynamics is the concept of path memory [11]. The walker dynamics is nonlocal in time and space; specifically, the instantaneous force acting on the drop depends on both its past and its environment. Since the pilot-wave originates from its previous bounces, the propulsive wave force depends on the walker's history. In prior work, where the wave field is modeled in terms of Bessel functions (see Ref. [9] and references therein) the memory enters through the dimensionless parameter $M_e = T_d/[T_F(1 - \Gamma/\Gamma_F)]$, where T_d is the decay time of unforced waves. The memory increases as $\Gamma \to \Gamma_F$, when the waves are more persistent. In the present work, where the wave generation is modeled explicitly, this parameter M_e does not arise in the theoretical formulation, but memory is naturally controlled through the vibrational acceleration Γ and the fluid viscosity ν.

In this article, we consider configurations with one or two cavities. The one-dimensional (1D) configuration has the attractive feature that it is restricted to normal incidence on the barrier, which is difficult to achieve in laboratory experiments [1]. The authors of that study state that "we can wonder if the output, reflection, or crossing is still probabilistic for a given angle" (p. 240401-3) and note that walkers with normal incidence have a higher probability of tunneling. Our 1D system necessarily treats only normal incidence, but nevertheless exhibits highly unpredictable tunneling events.

We consider the (free space) wave-particle model [10], here adapted to a 1D configuration and extended to permit domains of arbitrary cross section. The single-cavity configuration is displayed in Fig. 1. We choose a cavity of just a few Faraday wavelengths so that the droplet is strongly confined. In the two-cavity simulations, the droplet may cross the barrier and so tunnel from one cavity into the other (see Figs. 6 and 7). This highly confined configuration ensures that many tunneling attempts take place in a reasonable amount of time.

A. The wave-droplet model

The wave model consists of a weakly viscous quasipotential theory [10]. The wave elevation is denoted by $\eta(x,t)$ and the velocity potential, satisfying Laplace's equation in the fluid domain, by $\phi(x,z,t)$. The fluid has density ρ, surface tension σ, and kinematic viscosity ν. The free surface wave equations at $z = 0$ are given by

$$\frac{\partial \phi}{\partial t} = -g(t)\eta + \frac{\sigma}{\rho}\frac{\partial^2 \eta}{\partial x^2} + 2\nu\frac{\partial^2 \phi}{\partial x^2} - \frac{1}{\rho}P_d(x - X(t)), \tag{1}$$

$$\frac{\partial \eta}{\partial t} = \frac{\partial \phi}{\partial z} + 2\nu\frac{\partial^2 \eta}{\partial x^2}, \tag{2}$$

where the pressure term P_d in Eq. (1) indicates the presence of the droplet, which acts as a wave maker at $X(t)$ during the contact time. This wave system is coupled to the droplet's horizontal trajectory equation:

$$m\frac{d^2X}{dt^2} + cF(t)\frac{dX}{dt} = -F(t)\frac{\partial \eta}{\partial x}(X(t),t). \tag{3}$$

The magnitude of the propulsive wave force imparted during impact with the surface is prescribed by $F(t)$ and also appears in the damping coefficient. In a simplification of the model in Ref. [10], the forcing term $P_d(x - X(t))$ and the coefficient $F(t) = \int P_d dA$ are obtained by assuming that the droplet undergoes a periodic vertical motion, with period T_F, and that the bath surface acts on

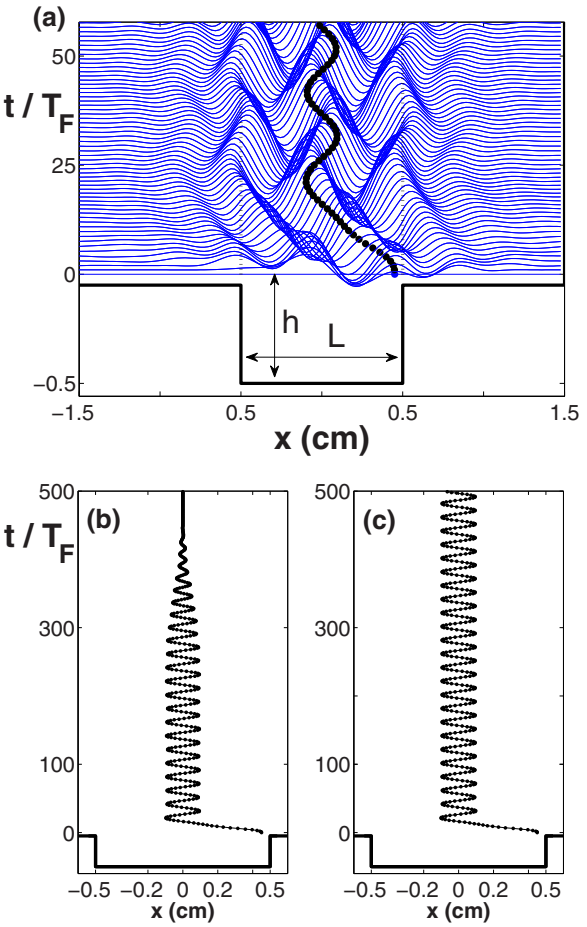

FIG. 1. (a) Cavity geometry: $L = 1$ cm, $h = 0.50$ cm, with an adjacent shallow region of depth 0.02 cm. Wave profiles are shown in units of T_F, at the phase when drop-bath contact is initiated. The Faraday wavelength is 0.47 cm. The thick curve indicates the horizontal position of the droplet. The sloshing of the pilot-wave promotes the oscillatory motion of the droplet. Panels (b) and (c): Hopf bifurcation apparent in a single cavity as the droplet evolves from a static bouncing state to an oscillating state with increasing Γ: (b) $\Gamma = 4.95$; (c) $\Gamma = 5.0$. The cavity shape is indicated at the bottom. The wave profiles in panels (b) and (c) were removed for the sake of clarity.

the droplet like a linear spring during the contact time $T_c = T_F/4$. In the present model $F(t) = (2\pi^2 mg/(\omega_0 T_c))\sin(\pi\tau(t)/T_c)$, where $\tau(t) = t \bmod (T_F)$ $(0 \leqslant \tau < T_c)$ and $F(t) = 0$ otherwise, namely when the droplet is in flight. These choices are consistent with experiments [12] and simulations of the full problem [10]. The wave-making term in (1) and the propulsive wave force in (3) are responsible for establishing the feedback between the waves and the droplet.

II. ONE-DIMENSIONAL MODEL REDUCTION AND NUMERICAL IMPLEMENTATION

This section describes the mathematical and numerical details used to solve the above system. The reader interested only in the results may proceed to Sec. III.

Let the two-dimensional fluid domain be denoted by $\Omega = \{(x,z), -L_T < x < L_T, -H(x) < z < 0\}$. At any time $t > 0$ the velocity potential $\phi(x,z,t)$ satisfies a boundary value problem, given

by Laplace's equation

$$\phi_{xx} + \phi_{zz} = 0, \quad (x,z) \in \Omega$$

in the interior of the fluid and a Neumann condition

$$\frac{d\phi}{dn} = 0$$

along the impermeable bottom located at $z = -H(x)$. At the ends of the fluid domain ($x = \pm L_T$, for L_T sufficiently large) the flow is assumed to be at rest. Therefore, computing the vertical speed $\phi_z(x,0,t)$ in Eq. (2) requires solving for the corresponding harmonic function in the fluid domain. Through a mathematical manipulation of this term, one can avoid solving the above elliptic boundary value problem within the fluid domain. A boundary (Fourier-type) operator is constructed, taking into account the harmonic properties of ϕ. Having this operator at hand, the two-dimensional model is reduced to an equivalent set of equations in one dimension. We now proceed to describing the construction of such an operator.

First, consider the conformal mapping from a uniform strip of unit height onto a corrugated strip, namely our physical domain with the cavities. The lower boundary is a polygonal line and the Schwarz-Christoffel mapping [13] is well suited in this case. Consider these two strips in the complex plane. The uniform strip, our canonical domain, is in the complex w plane, where $w = \xi + i\zeta$. The physical domain is in the complex Z plane, where $Z = x + iz$. The mapping is given by the complex function $Z = F(w)$, where $|dZ/dw|^2$ is equal to the Jacobian $|J|$ of the corresponding change of variables. The harmonic functions $x = x(\xi,\zeta)$ and $z = z(\xi,\zeta)$ satisfy the Cauchy-Riemann equations and therefore $|J| = x_\xi^2 + x_\zeta^2$. It also follows for the velocity potential that

$$\phi_\xi(x,z) = \phi_x x_\xi + \phi_z z_\xi, \quad \phi_\zeta(x,z) = \phi_x x_\zeta + \phi_z z_\zeta.$$

By inverting a linear system [14], one obtains

$$\phi_z = \frac{1}{|J|}[-x_\zeta \phi_\xi + x_\xi \phi_\zeta].$$

This relation will be used for the Dirichlet-to-Neumann (DtN) boundary operator. The undisturbed free surface in the physical and canonical domains are given by $z = 0$ and $\zeta = 1$ respectively. Therefore $x_\zeta(\xi,1) \equiv 0$ and the Jacobian is given by $|J|(\xi,1) = x_\xi^2(\xi,1) \equiv M^2(\xi)$. We define $M(\xi)$ as our metric coefficient along the undisturbed free surface. Computing the vertical speed along the free surface amounts to

$$\phi_z = \frac{1}{M(\xi)}\phi_\zeta. \tag{4}$$

We are now in a position to express the vertical speed ϕ_z only with information along the undisturbed free surface, namely without solving Laplace's equation in the fluid domain. Recall that as a result of the conformal mapping, the velocity potential ϕ is a harmonic function in both the physical and the canonical domains. In the canonical domain (in the w plane) the DtN operator is trivially obtained from the Fourier representation of the corresponding Dirichlet data. In the w plane, our time-dependent Dirichlet data $\phi(x(\xi,1),0,t) = \varphi(\xi,t)$ are represented by

$$\varphi(\xi,t) = \frac{1}{\sqrt{2\pi}} \int_{-\infty}^{\infty} \hat{\varphi}(k,t) e^{ik\xi} dk.$$

Using separation of variables we perform the harmonic extension of the Dirichlet data into the unit strip, then differentiate in ζ, which yields the Dirichlet-to-Neumann operator in the w plane:

$$\phi_\zeta(\xi,1,t) = DtN_w[\varphi](\xi,t) \equiv \frac{1}{\sqrt{2\pi}} \int_{-\infty}^{\infty} k \tanh(k) \hat{\varphi}(k,t) e^{ik\xi} dk. \tag{5}$$

Using expressions (4) and (5), the variable-depth problem is (analytically) reduced to one dimension, in terms of x along the undisturbed surface. In the physical domain, we have that

$$DtN_Z[\varphi](x,t) = \phi_z(x,0,t) = \frac{1}{M(\xi(x,0))} DtN_w[\varphi](\xi(x,0)). \tag{6}$$

The notation indicates that the DtN operator is first computed in the w plane in terms of the ξ variable [as given in Eq. (5)], but needs to be evaluated in the physical domain. This final step makes use of the relation $\xi = \xi(x,0)$, the real part of the inverse-map evaluated along the undisturbed free surface. In other words, given a set of uniformly distributed points x_j in the physical domain, we will need to know their preimages, $\xi_j = \xi(x_j,0)$, in the canonical domain in order to evaluate the vertical speeds there and rescale accordingly, using the reciprocal of the metric coefficient M.

It is also instructive to look at the long-wave (shallow-water) regime of this problem, even though we operate in the intermediate-depth regime within each cavity. For clarity we remove the shaking, the droplet, and surface tension effects. Consider the linear potential theory, wave problem, given by

$$\phi_t = -g\eta, \tag{7}$$

$$\eta_t = \phi_z, \tag{8}$$

where $\phi(x,z,t)$ is harmonic in our fluid domain (the corrugated strip) together with a Neumann condition at the impermeable bottom. The initial conditions are $\phi(x,0,0) = \varphi_0(x)$ and $\eta(x,0) = \eta_0(x)$. Using the formulation discussed above, the dynamics can be reduced completely to the free surface. In other words, we write that

$$\varphi_t = -g\eta, \tag{9}$$

$$\eta_t = \frac{1}{\sqrt{2\pi}M(\xi(x,0))} \int_{-\infty}^{\infty} k\tanh(k)\hat{\varphi}(k,t)e^{ik\xi(x,0)}dk, \tag{10}$$

where the initial Dirichlet data is $\varphi(x,0) = \varphi_0(x)$ and the initial wave profile is $\eta(x,0) = \eta_0(x)$. Eliminating η from this system yields

$$\varphi_{tt} + \frac{g}{\sqrt{2\pi}M(\xi(x,0))} \int_{-\infty}^{\infty} k\tanh(k)\hat{\varphi}(k,t)e^{ik\xi(x,0)}dk = 0.$$

In the long-wave limit $k\tanh(k) \sim -(ik)^2$ and the equation reduces to

$$\varphi_{tt} - \frac{g}{M(\xi(x,0))}\varphi_{\xi\xi} = 0.$$

Recalling that $\phi_\xi = M(\xi(x,0))\phi_x$, we have the long-wave equation

$$\varphi_{tt} - g\{M(\xi(x,0))\varphi_x\}_x = 0 \tag{11}$$

in the physical domain. Therefore, in the long-wave limit, the presence of the cavities (encoded in the metric term M) corresponds to a variable speed in the wave equation (11). Consider the wave model used in Refs. [3,4] and, for clarity, remove the shaking, the droplet, and surface tension effects. It can be recast in the form

$$\phi_{tt} - g\nabla\cdot[b(x,y)\nabla\phi] = 0, \tag{12}$$

where a piecewise constant b is used, matching the Faraday wave speeds at the barrier's different depths. This nearly monochromatic model is not a shallow water model, but is of the same class as (11).

The Fourier integral in (5) represents a pseudodifferential operator with the symbol (i.e., Fourier multiplier) equal to $k\tanh(k)$. In our wave regime of interest the symbol cannot be simplified. The underlying effect of the barrier, through its width and height, comes into the model through the

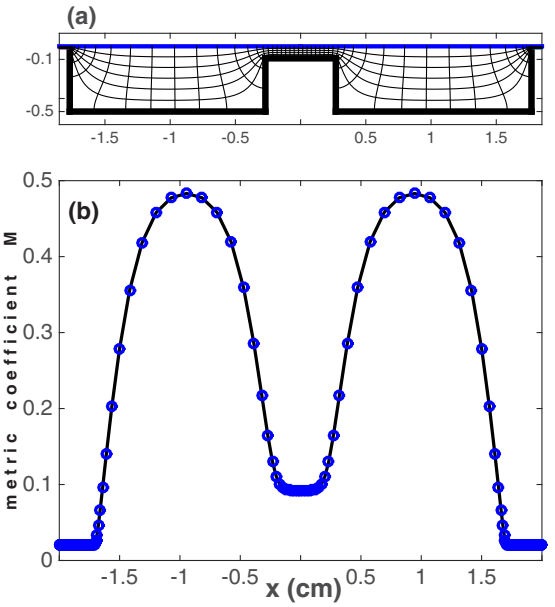

FIG. 2. (a) Two cavities with the level curves from the ξ-ζ coordinate system in the canonical domain: $L = 1.5$ and $L_b = 0.4$. Each vertical curve arises by setting $\xi(x,y)$ constant, while each horizontal curve represents the level curve given by $\zeta(x,y)$ constant. In the canonical domain these lines represent a uniform Cartesian grid. Along the undisturbed free surface, the corresponding grid-point spacing is highly nonuniform. The same effect happens in the canonical domain when starting with a uniform grid in x. In the middle of each cavity, as well as in the middle of the barrier, the Jacobian matrix is approximately a multiple of the identity. The mesh is almost Cartesian. There the metric coefficient M is approximately constant, as shown in panel (b). Near the ends of the cavities, M is highly variable, thus affecting the wave speed and promoting wave reflection.

Fourier integral in a nontrivial fashion, both through the metric term M as well as the $\xi = \xi(x,0)$ relation. In Fig. 2(a) we have two cavities with a barrier. The Cartesian ξ-ζ coordinate system in the w plane becomes a highly distorted (orthogonal) curvilinear coordinate system in the Z plane. In Fig. 2(b) the metric coefficient M, related to the Jacobian, is graphed as a function of x. Given a uniform grid ξ_m we have displayed $M_m = M(\xi(x_m,0))$ in the physical domain, noting the irregular spacing of the markers.

The spatial derivatives of Eqs. (1)–(3) are computed using a Fourier spectral method. The shallow regions, seen on the sides of the cavity in Fig. 1(a), extend sufficiently far that periodic boundary conditions may be applied at the ends of the horizontal domain. The normal velocity $\phi_z(x,0,t)$ is computed with a fast Fourier transform (FFT) through the Dirichlet-to-Neumann operator.

As described above, the DtN operator is computed in steps. Owing to depth variations in the fluid domain, the conformal mapping is computed using the Schwarz-Christoffel Toolbox (SCT) [13], which numerically maps a polygonal-shaped (2D) fluid domain onto a flat strip of unit height [14,15]. The SCT chooses the origin to be at the bottom and the undisturbed free surface to be at $\zeta \equiv 1$. The mapping $Z = F(w)$ is computed only once, at the beginning of a simulation. Commands are readily available [16] to compute the Jacobian as well as $\xi_j = \xi(x_j,0)$ on a given grid. Note that we use the mapping $\xi_j \leftrightarrow x_j$ established at the beginning of a given simulation. We use FFTs to compute the vertical speed (6) in the physical domain:

$$\phi_z(x,0,t) = DtN_Z[\phi](x,t) = \{\mathcal{F}^{-1}[G(k)\mathcal{F}(\phi)]\}/M(\xi(x,0)),$$

where $\mathcal{F}$ indicates an FFT in the ξ coordinate. Recall that the Fourier multiplier is $G(k) = k\tanh k$.

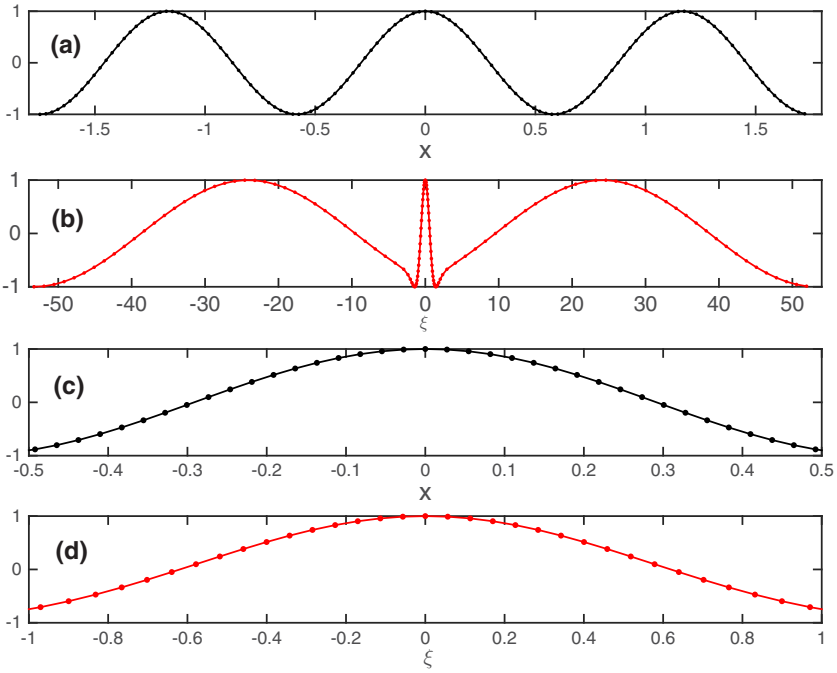

FIG. 3. We consider a single cavity of depth $h = 0.5$ cm. (a) A single Fourier mode $f(x) = \cos(6\pi x/(2L_T))$ along the free surface $z = 0$, where $2L_T$ is the total length of our computational domain. (b) The above Fourier mode is displayed along the nodes' preimages ξ_j in the canonical domain. Namely, the mode is expressed as $F(\xi) = f(x(\xi,1)) = \cos(6\pi x(\xi,1))/(2L_T)$. This function is not represented by a single mode in ξ. (c) A detail of panel (a) in the middle of the cavity. (d) A detail of panel (b) in the corresponding region of panel (c) where the Jacobian is approximately 2. Note that in this region panel (d) shows merely a rescaling of panel (c). The nodes are (approximately) uniformly spaced.

It is important to recall that for a given uniform grid $x_j (j = 1, \ldots, J)$ along the free surface in the physical domain, the conformal mapping generates a nontrivial distortion in the canonical domain, as expressed through the real part of the inverse map $\xi_j = \xi(x_j,0)$. This distortion gives rise to grid points ξ_j distributed in a very irregular fashion. The Fourier integral given in (5) is computed with an FFT, which uses equally spaced points, and therefore the corresponding Dirichlet data φ_j needs to be interpolated on a uniform grid in ξ. This interpolation is done through the use of cubic splines. In order to describe the main ideas, consider the following simple example with the single cavity shown in Fig. 1. Take a single Fourier mode along the physical free surface, which in the canonical domain is no longer monochromatic, for example, $F(\xi) = \exp(ikx(\xi,1))$. For graphing purposes, we consider the Fourier mode $f(x) = \cos(6\pi x_j/(2L_T))$, where $2L_T$ is the total length of our computational domain. In Fig. 3(a) this function is displayed at the corresponding grid points x_j. This function is not monochromatic in ξ, as is clearly evident in Fig. 3(b). In Fig. 3(c) we show a detail in the interval $x \in [-0.5,0.5]$, inside the cavity, where the Jacobian is approximately equal to 0.5. Comparing with the detail of Fig. 3(d), we see that, in this region, there is merely a rescaling (by a factor of 2) of the node spacing in this region. In the case of two cavities, Fig. 2 displays, in both Figs. 2(a) and 2(b), how a uniform grid in ξ becomes highly distorted in the physical domain.

Keeping in mind this simple example where a monochromatic mode gets modulated in frequency, we perform an oversampling of grid points in our numerical method when using the cubic splines. This procedure generates additional grid point values of $\exp(ikx(\xi,1))$ on a finer uniform grid $\xi_m (m = 1, \ldots, MJ)$, where $M \geqslant 1$ indicates the oversampling rate. In our simulations we used

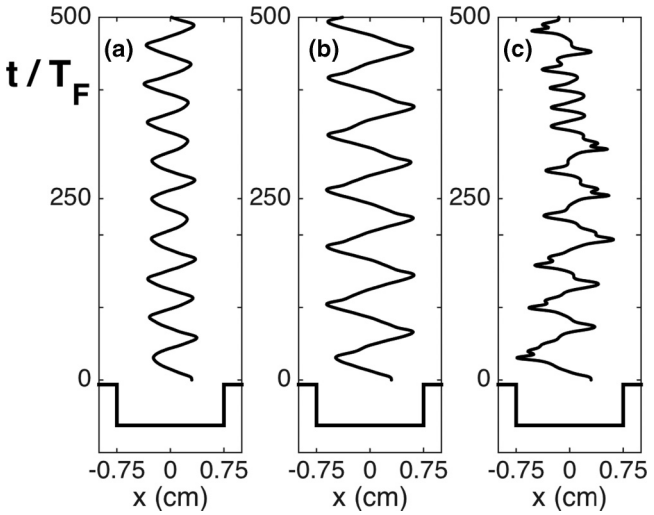

FIG. 4. A single cavity of length $L = 1.5\,\text{cm}$ and depth $h = 0.5\,\text{cm}$. Three vertical accelerations are considered. (a) $\Gamma = 4.4$ yields an oscillatory droplet motion in the middle of the cavity. (b) When $\Gamma = 4.7$ the oscillatory droplet motion approaches the cavity's boundaries. (c) When $\Gamma = 5.2$, the onset of chaotic droplet motion is apparent.

$J = 128$ and $M = 4$. On the uniform grid ξ_m, FFTs are used to compute the Fourier integral corresponding to the DtN operator in the canonical domain. Through the use of cubic splines, the Neumann data, found on the uniform grid points ξ_m, is interpolated onto the nonuniform grid points $\xi(x_j,0)$, namely the preimage of the original uniform grid points in the physical domain.

In summary the geometrical information of the cavities and barriers is encoded in the variable (metric) coefficient M and through the relation $\xi_j = \xi(x_j,0)$ which are defined along the undisturbed free surface, when a simulation starts. The dynamics is thus reduced to a one-dimensional problem containing depth effects. The time evolution is performed with a second-order fractional-step Verlet method.

III. RESULTS

The physical parameters are taken in the same range as in Ref. [10]: droplet radius $R_o = 0.035$ cm, $\sigma = 20.9\,\text{dyn cm}^{-1}$, $\nu = \mu/\rho = 0.16\,\text{cm}^2\,\text{s}^{-1}$, $\rho = 0.95\,\text{g cm}^{-3}$, and forcing frequency $\omega_o = 80\,\text{Hz}$. The corresponding Faraday wavelength is $\lambda_F \approx 0.47\,\text{cm}$. We adopt boundaries comparable to those examined in the laboratory: Adjacent to the main cavity is a shallow region that eliminates the meniscus on the side walls that would otherwise arise. Since the droplet cannot walk in sufficiently shallow layers, it is generally repelled by submerged boundaries [3]. The pronounced decay of waves over the shallow region is evident in Fig. 1(a).

A. Single cavity

We first consider a droplet confined to a single cavity of size 1 cm $\approx 2\lambda_F$ [see Fig. 1(a)]. As the forcing amplitude Γ increases, a Hopf bifurcation arises, as depicted in Figs. 1(b) and 1(c). When $\Gamma = 4.95$, the droplet drifts towards a static bouncing state at the center of the cavity and the waves converge to a standing wave form. In the position-velocity phase space, the droplet spirals towards a critical point. With the same initial conditions, at $\Gamma = 5.0$, the droplet now executes a regular oscillatory trajectory corresponding to a limit cycle in phase space. In this case, the wave profiles are continuously sloshing in the strobed visualization, as is evident in Fig. 1(a). In a sense,

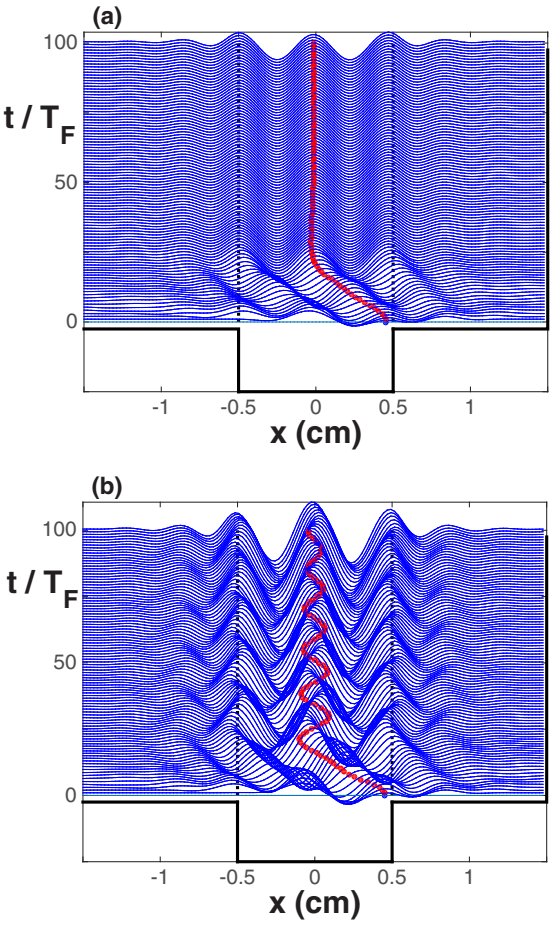

FIG. 5. Two different cavity depths h are considered. Cavity geometry: $L = 1$ cm with an adjacent shallow region of depth 0.02 cm. The vertical acceleration parameter $\Gamma = 5.3$ is slightly stronger than in Fig. 1. Wave profiles are shown in increments of T_F. (a) A shallow cavity where the depth is equal to $h = 0.10$ cm. Even with a stronger shaking, the droplet goes directly to a static bouncing state, guided by the underlying field, which becomes a standing wave. This depth is not favorable to walking and therefore, in the case with two cavities, the fluid depth over the barrier will be $h_b = 0.092$ cm. (b) The depth in the cavity is equal to $h = 0.25$ cm. The droplet gradually evolves to a bouncing state.

the wave is acting as a time-periodic potential for the oscillating droplet. A well-known example of a particle under the effect of an oscillating potential is Duffing's equation; however, the potential and its corresponding time dependence are prescribed from the start. For example, switch off the feedback and prescribe the wave profile in the droplet trajectory equation. Motivated by Fig. 1, we choose $\eta = V(X,t) = a[1 + \cos((2\pi/\lambda_F)X - \varepsilon \sin(\omega_s t))]$, a monochromatic sloshing wave with sloshing frequency ω_s and amplitude ε. The time-varying potential $V(X,t)$ thus plays the role of the wave η in the damped oscillator (3). Expanding dV/dX in ε yields a generalized version of a periodically forced Duffing's equation, which is known to yield chaos. Likewise, increasing Γ in our model leads to chaotic motion of the droplet. For the wave-droplet association, the underlying potential is dynamically generated rather than prescribed: The nature of the underlying wave field is not known *a priori* and the pilot-wave problem is intrinsically more difficult. Nevertheless, in the

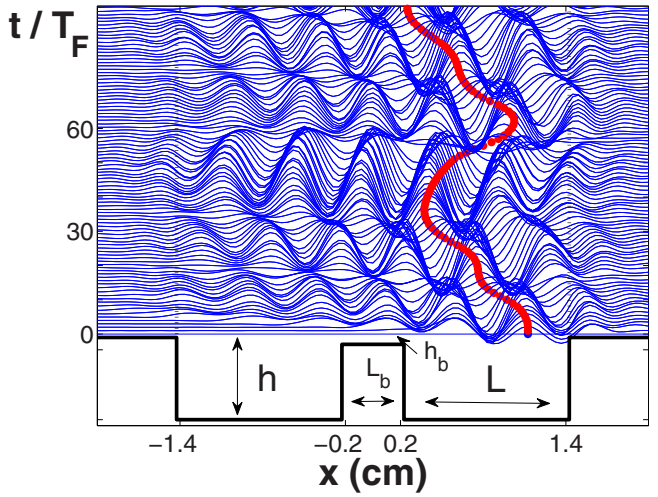

FIG. 6. Two cavities of width $L = 1.2$ cm and depth $h = 0.5$ cm, separated by a barrier of width $L_b = 0.4$ cm and depth $h_b = 0.092$ cm. The forcing amplitude is $\Gamma = 4.6$ with $\Gamma_F \approx 5$ for the present geometry.

regime displayed in Fig. 1(a), characterized by the periodic wave sloshing, it resembles a periodically varying potential.

The range of the droplet's oscillations is limited by the sloshing wave field which transfers to the droplet information about the cavity's boundaries. At higher memory, this is not the case, as is evident in Fig. 4. In Fig. 4(b), at a higher vertical acceleration, the oscillatory droplet motion approaches the boundaries of the cavity. The onset of a chaotic trajectory, observed at higher Γ, is depicted in Fig. 4(c).

B. Two cavities separated by a barrier

The choices of cavity length and barrier width were made based on the simulations presented above, while noting that combining two cavities reduces the Faraday threshold even in the presence of a high barrier. We want the barrier to be a forbidden walking region. The barrier depth is chosen accordingly. In Ref. [1], the barrier depth was $h_b = 0.1$ cm. In Fig. 5(a) we consider a single cavity with depth $h = 0.1$ cm. Even with a stronger forcing of $\Gamma = 5.3$ the droplet moves directly to a static bouncing state in the middle of the cavity. When the depth is increased to $h = 0.25$ cm the droplet moves towards a bouncing state in an oscillatory fashion. These examples play a role in our choice for the tunneling simulations. We first investigated tunneling events for a (reference) barrier width of $L_b = 0.40$ cm [1]. We chose the barrier depth of $h_b = 0.092$ cm, slightly smaller than that considered in the experiments, since it lead to a tunneling probability on the order of 50% for a cavity size of $L = 1.2$ cm and 25% for $L = 1.5$ cm.

We now examine this model's ability to capture tunneling. In Ref. [1], the tunneling behavior was characterized in terms of the barrier width and walker speed. Since the free walker speed is prescribed by Γ [9], we will use Γ as the control parameter in our simulations. Figure 6 displays the geometry used in our study of tunneling. Two cavities of width L and depth h are separated by a barrier of width L_b and depth h_b. When $\Gamma = 4.6$, tunneling takes place relatively often. For $\Gamma \leqslant 4.3$, the droplet never escapes its initial cavity.

In Fig. 7, we compare the droplet trajectory for two different values of the barrier width L_b. All other system parameters are kept the same, including the droplet's initial position within the cavity. The tunneling pattern, as well as the tunneling probability, change dramatically in response to a small change in L_b. As in Ref. [1], the probability of tunneling is here defined as the ratio between the total number of tunneling events divided by the total number of attempts. A detail of the wave

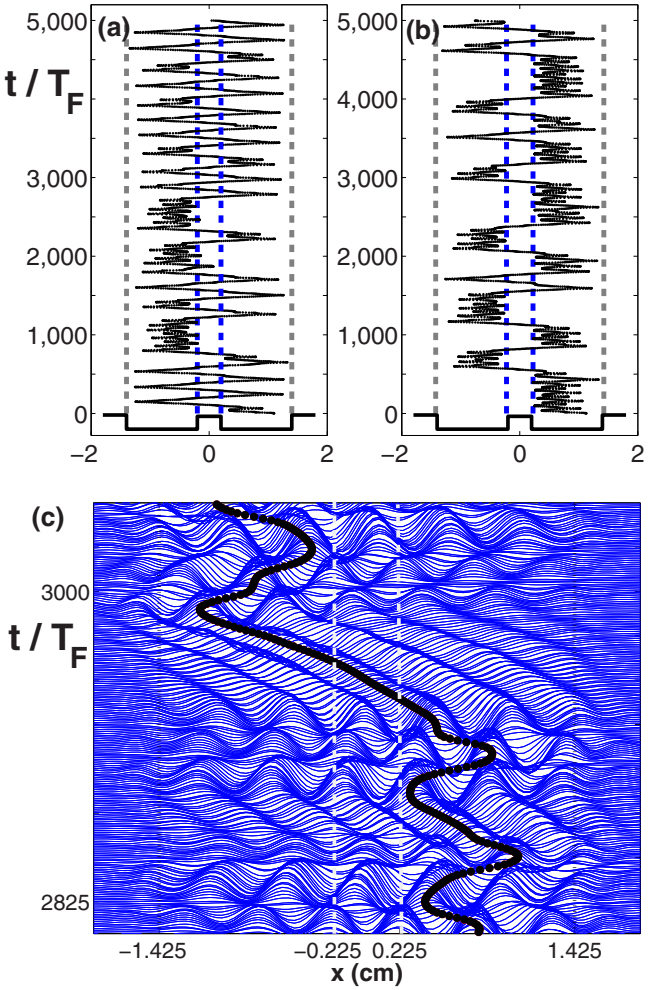

FIG. 7. Droplet tunneling at $\Gamma = 4.6$. Cavity geometry as in Fig. 6: $L = 1.2\,\text{cm}, h = 0.5\,\text{cm}, h_b = 0.092\,\text{cm}$. Observed Faraday threshold $\Gamma_F \approx 5$. (a) $L_b = 0.4\,\text{cm}$ with tunneling probability of 58%; (b) $L_b = 0.45\,\text{cm}$ with tunneling probability of 19%. Same initial conditions. (c) The wave field in an interval from panel (b) that includes a tunneling event.

field in Fig. 7(b) is displayed in Fig. 7(c). There is a robust feature common to all of our simulations with two cavities: A failed attempt to tunnel is generally accompanied by a pronounced standing wave in the neighboring cavity (see Figs. 6 and 7) that serves to block the tunneling attempt.

Figure 8(a) shows the exponential decay of the tunneling probability with barrier width L_b, for two different barrier configurations. The cavity widths were taken to be $L = 1.5\,\text{cm}$, while the barrier depth was taken to be $h_b = 0.092\,\text{cm}$ (depicted with triangles) and $h_b = 0.090\,\text{cm}$ (depicted with squares). The number of attempts depends on the cavity width and for $L = 1.5\,\text{cm}$ we observed an average of 55 attempts per simulation. We first considered $h_b = 0.092\,\text{cm}$, and observed the exponential decay of the tunneling probability from approximately 65% to 2%, as the barrier width increases from 0.36 to 0.52 cm. Note that we do not expect the 1D dynamical model reported herein to be in quantitative agreement with 2D laboratory experiments in Ref. [1]. The least-squares fit is satisfactory, and the exponential decay rate does not change much as we change the barrier's depth. For a higher (shallower) barrier ($h_b = 0.090\,\text{cm}$), the tunneling probability is evidently smaller and

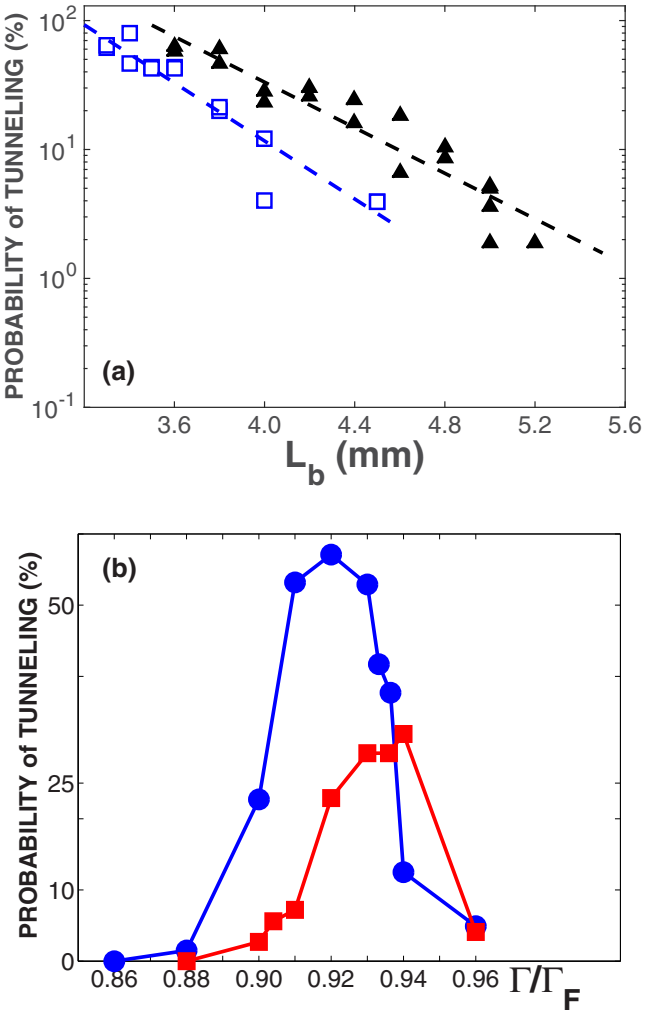

FIG. 8. (a) Exponential decay of tunneling probability with barrier width L_b. Two cavities of width $L = 1.5$ cm each, are considered. The barrier depth is $h_b = 0.092$ cm (triangles) and $h_b = 0.090$ cm (squares). The time interval is $5000T_F$ for all observations reported. At least two different initial droplet positions were considered for each barrier width. At $L_b = 5.2$ mm the second simulation (for a triangle) displayed no tunneling events. In the presence of a shallower barrier, as depicted with squares, tunneling stopped completely beyond a barrier of width $L_b = 4.7$ mm, within our number of attempts. The lines represent the corresponding least-squares fit. (b) The dependence of tunneling probability on memory for two cavities of width $L = 1.2$ cm and barrier widths $L_b = 0.40$ cm (circles) and $L_b = 0.50$ cm (squares). The optimal tunneling regime is evident near $\Gamma/\Gamma_F = 0.92$, where $\Gamma_F \approx 5$.

the model responds accordingly, as shown by the square markers. Despite the configuration not being semi-infinite, as is usual in the quantum tunneling problem, we observed exponential decay with barrier width, except for specific cases where resonance arises: The small cavity length together with the barrier width are a multiple of the Faraday wavelength, allowing for substantial forcing of blocking waves in the other cavity. These resonant cases were more common for a cavity of length $L = 1.2$ cm, where the average number of tunneling attempts (per simulation) was of the order of 80.

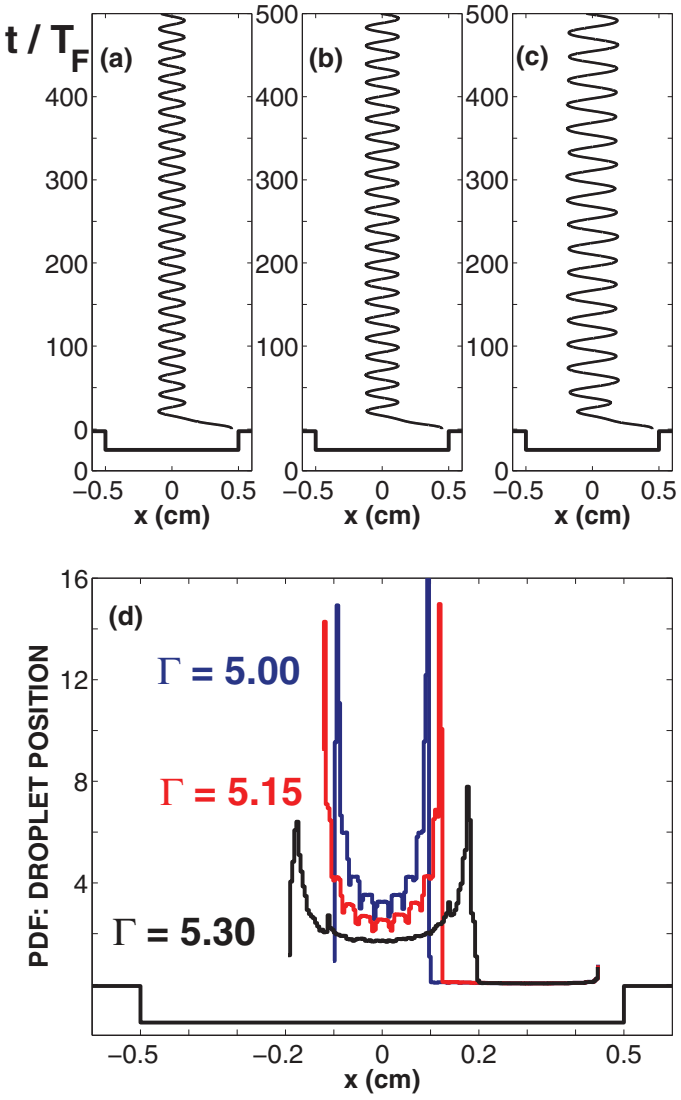

FIG. 9. Single-cavity oscillations: (a) $\Gamma = 5.0$; (b) $\Gamma = 5.15$; (c) $\Gamma = 5.3$. All with initial position at $x = 0.45$. (d) Histograms for periodic droplet motion reported in panels (a)–(c). Here $\Gamma_F \approx 6.1$.

Our theoretical model also leads to an interesting prediction. Figure 8(b) indicates an optimal Γ for tunneling, above which blocker waves in the target cavity forbid it. Close to the Faraday threshold, the prevalence of standing waves in the target cavity blocks most tunneling attempts.

In Fig. 9, we display the oscillatory motion of a droplet confined to a single cavity ($L = 1.0$ cm) for three values of Γ. Histograms of the droplet position are presented in Figs. 9(d). In Fig. 10, we display the probability density function (PDF) for a droplet walking between two cavities of $L = 1.2$ cm and barrier depth $h_b = 0.092$ cm. We consider the case where tunneling is relatively unlikely (19%), as in Fig. 7(b). In Fig. 10(a) we present the results of a long simulation up to a time $t = 25000T_F$, for which 25 million droplet positions are recorded. In Fig. 10(b) we consider the same configuration but for 12 different initial droplet positions, 6 in each cavity. A single realization is displayed in Fig. 10(c), where the droplet is found more often in the right cavity. Each simulation

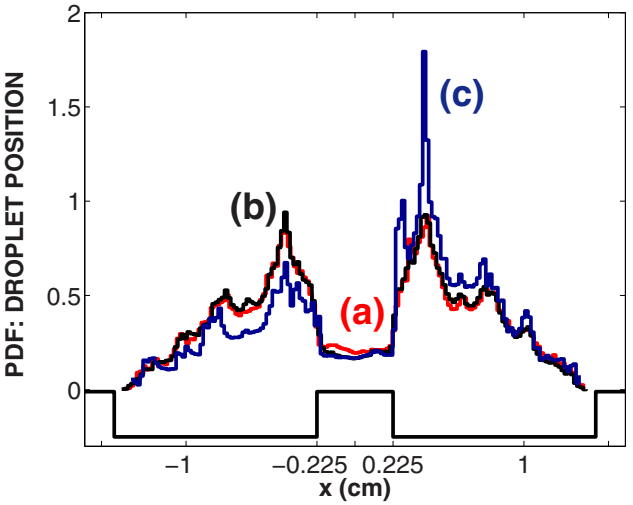

FIG. 10. Histograms of droplet position. Here, $\Gamma = 4.6$, $\Gamma_F \approx 5$, $L = 1.2\,\text{cm}$, $L_b = 0.45\,\text{cm}$ and depth $h_b = 0.092\,\text{cm}$. (a) PDF for a single simulation with $t \in [0, 25000T_F]$. (b) PDF for 12 simulations with different initial droplet positions (6 in each cavity) and $t \in [0, 5000T_F]$. (c) PDF for a single realization from the 12 simulations.

extends over $5000T_F$. For each starting point, 5 million droplet positions are recorded and then superposed. The PDFs in Figs. 6(a) and 6(b) are remarkably similar, suggesting the possibility of a stationary ergodic process for the random tunneling events and related droplet positions. This behavior is also apparent for other Γ values, as shown in Fig. 11, where only 6 initial positions were taken, but the limiting pattern of the PDF is already emerging. We have reduced both the forcing Γ and the barrier width L_b relative to Fig. 10.

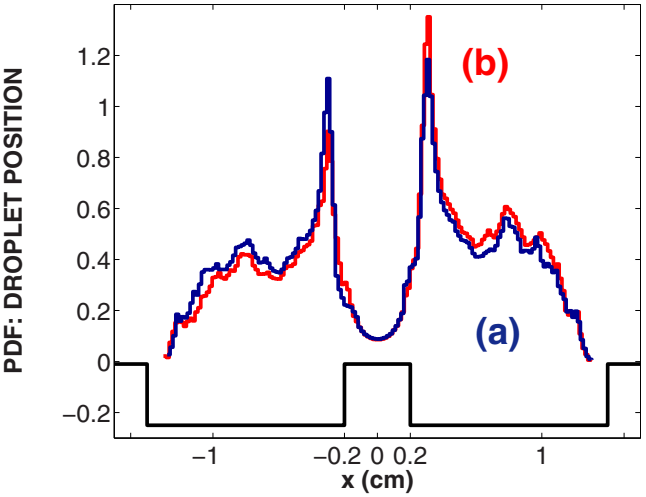

FIG. 11. Histograms of droplet position. Here, $\Gamma = 4.5$, $\Gamma_F \approx 5$, $L = 1.2\,\text{cm}$, $L_b = 0.40\,\text{cm}$, and depth $h_b = 0.092\,\text{cm}$. (a) PDF for a single simulation with $t \in [0, 30\,000\,T_F]$. (b) PDF for only 6 simulations with different initial droplet positions (3 in each cavity) and $t \in [0, 5000\,T_F]$.

IV. CONCLUSIONS AND FUTURE DIRECTIONS

We have presented a theoretical model capable of describing 1D pilot-wave dynamics over variable bottom topography. We have used it to explore the dynamics and statistics of tunneling and walker motion in a confined domain. In a single cavity, the droplet behaves as an oscillator that transitions into a chaotic trajectory at sufficiently high memory.

When two cavities are considered, tunneling simulations confirm that our theoretical model captures the exponential decay of the crossing probability with increasing barrier width [1]. Tunneling simulations also indicate an optimal memory range for crossing due to the prevalence of blocker waves in the target cavity at high memory. In Ref. [17], the authors studied the phenomenon of quantum tunneling across a symmetric double-well potential perturbed by a monochromatic driving force. Playing a role roughly analogous to the blocker waves in our hydrodynamic pilot-wave system, this periodic driving leads to the "coherent destruction of tunneling," as defined by the authors.

Finally the statistical behavior of our system, specifically the emergence of a robust PDF, suggests an underlying stationary ergodic process. While we do not expect the 1D dynamical model reported herein to be in quantitative agreement with 2D laboratory experiments, we believe that it has considerable potential in establishing the connection between chaotic particle-wave dynamics and emergent quantum-like statistics, as has been reported in a number of hydrodynamic quantum analog systems [5,18,19].

ACKNOWLEDGMENTS

The authors would like to thank the referees for their valuable comments. The authors would also like to thank Dr. C. Galeano-Ríos (IMPA), Dr. G. Pucci, Dr. L. Faria, and M. Biamonte (MIT) for their comments. A.N. was supported by CNPq under (PQ-1B) 301949/2007-7, FAPERJ *Cientistas do Nosso Estado* Project No. 102.917/2011 and the MIT-Brazil Program. A.N. is grateful to the University of Bath Mathematics Department and to the MIT Mathematics Department for hosting him as a visiting professor during periods of this research. P.A.M. gratefully acknowledges support through the Royal Society Wolfson award and the EPSRC Project No. EP/N018176/1. J.W.M.B. was supported by NSF through Grants No. CMMI-1333242 and No. DMS-1614043, the MIT-Brazil Program, and the CNPq-Science without Borders Award No. 402300/2012-2.

---

[1] A. Eddi, E. Fort, F. Moisy, and Y. Couder, Unpredictable Tunneling of a Classical Wave-Particle Association, Phys. Rev Lett. **102**, 240401 (2009).

[2] G. Gamow, The quantum theory of nuclear desintegration, Nature (London) **122**, 805 (1928).

[3] G. Pucci, P. Sáenz, L. M. Faria, and J. W. M. Bush, Non-specular reflection of walking droplets, J. Fluid Mech. **804**, R3 (2016).

[4] L. M. Faria, A model for Faraday pilot waves over variable topography, J. Fluid Mech. **811**, 51 (2017).

[5] D. M. Harris, J. Moukhtar, E. Fort, Y. Couder, and J. W. M. Bush, Wavelike statistics from pilot-wave dynamics in a circular corral, Phys. Rev. E **88**, 011001 (2013).

[6] B. Benjamin and F. Ursell, The stability of the plane free surface of a liquid in a vertical periodic motion, Proc. Royal Soc. **225**, 505 (1954).

[7] J. Walker, Drops of liquid can be made to float on the liquid: What enables them to do so? Sci. Am. **238**, 151 (1978).

[8] Y. Couder, S. Protière, E. Fort, and A. Boudaoud, Walking and orbiting droplets, Nature (London) **437**, 208 (2005).

[9] J. W. M. Bush, Pilot-wave hydrodynamics, Ann. Rev. Fluid Mech. **47**, 269 (2015).

[10] P. A. Milewski, C. A. Galeano-Rios, A. Nachbin, and J. W. M. Bush, Faraday pilot-wave dynamics: modelling and computation, J. Fluid Mech. **778**, 361 (2015).

[11] A. Eddi, E. Sultan, J. Moukhtar, E. Fort, M. Rossi, and Y. Couder, Information stored in Faraday waves: The origin of a path memory, J. Fluid Mech. **674**, 433 (2011).
[12] J. Molacek and J. W. M. Bush, Drops walking on a vibrating bath: Towards a hydrodynamic pilot-wave theory, J. Fluid Mech. **727**, 612 (2013).
[13] T. A. Driscoll and L. N. Trefethen, *Schwarz-Christoffel Mapping* (Cambridge University Press, Cambridge, UK, 2002).
[14] A. Nachbin, A terrain-following Boussinesq system, SIAM J. Appl. Math. **63**, 905 (2003).
[15] W. Artiles and A. Nachbin, Nonlinear Evolution of Surface Gravity Waves Over Highly Variable Depth, Phys. Rev. Lett. **93**, 234501 (2004).
[16] A. Fokas and A. Nachbin, Water waves over a variable bottom: A non-local formulation and conformal mappings, J. Fluid Mech. **695**, 288 (2012).
[17] F. Grossmann, T. Dittrich, P. Jung, and P. Hanggi, Coherent Destruction of Tunneling, Phys. Rev. Lett. **67**, 516 (1991).
[18] S. Perrard, M. Labousse, M. Miskin, E. Fort, and Y. Couder, Self-organization into quantized eigenstates of a classical wave-driven particle, Nat. Commun. **5**, 3219 (2014).
[19] D. M. Harris and J. W. M. Bush, Droplets walking in a rotating frame: From quantized orbits to multimodal statistics, J. Fluid Mech. **739**, 444 (2014).